Tuning the Self-Assembly of Short Peptides via Sequence Variations

Yurong Zhao,[†] Jiqian Wang,[†] Li Deng,[†,‡] Peng Zhou,[†] Shengjie Wang,[†] Yanting Wang,[‡] Hai Xu,*,[†] and Jian R. Lu*,[§]

[†]Centre for Bioengineering and Biotechnology, China University of Petroleum (East China), 66 Changjiang West Road, Qingdao 266580, People's Republic of China

[‡]State Key Laboratory of Theoretical Physics, Institute of Theoretical Physics, Chinese Academy of Sciences, 55 East Zhongguancun Road, Post Office Box 2735, Beijing 100190, People's Republic of China

[§]Biological Physics Group, School of Physics and Astronomy, University of Manchester, Manchester M13 9PL, United Kingdom

S *Supporting Information*

ABSTRACT: Peptide self-assembly is of direct relevance to protein science and bionanotechnology, but the underlying mechanism is still poorly understood. Here, we demonstrate the distinct roles of the noncovalent interactions and their impact on nanostructural templating using carefully designed hexapeptides, $I_2K_2I_2$, I_4K_2, and KI_4K. These simple variations in sequence led to drastic changes in final self-assembled structures. β-sheet hydrogen bonding was found to favor the formation of one-dimensional nanostructures, such as nanofibrils from I_4K_2 and nanotubes from KI_4K, but the lack of evident β-sheet hydrogen bonding in the case of $I_2K_2I_2$ led to no nanostructure formed. The lateral stacking and twisting of the β-sheets were well-linked to the hydrophobic and electrostatic interactions between amino acid side chains and their interplay. For I_4K_2, the electrostatic repulsion acted to reduce the hydrophobic attraction between β-sheets, leading to their limited lateral stacking and more twisting, and final fibrillar structures; in contrast, the repulsive force had little influence in the case of KI_4K, resulting in wide ribbons that eventually developed into nanotubes. The fibrillar and tubular features were demonstrated by a combination of cryogenic transmission electron microscopy (cryo-TEM), negative-stain transmission electron microscopy (TEM), and small-angle neutron scattering (SANS). SANS also provided structural information at shorter scale lengths. All atom molecular dynamics (MD) simulations were used to suggest possible molecular arrangements within the β-sheets at the very early stage of self-assembly.
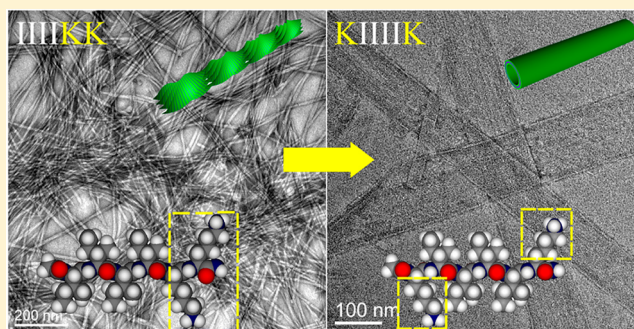
1. INTRODUCTION

Self-assembly is ubiquitous in biological systems and has been extensively exploited as a potential strategy to fabricate structurally well-defined patterns and functions from simple building blocks.[1−3] Because of their biocompatibility and chemical diversity, peptides are of particular interest, and their assembled materials can be endowed with various biological characteristics, such as biodegradability and biofunctionality, through appropriate molecular design.[4−14] Although noncovalent forces between complementary interacting molecular surfaces are known to play a crucial role in mediating peptide self-assembly processes and structures, a thorough understanding of these interactions and their cooperativity is still lacking. Consequently, most known self-assembling peptides have either been discovered serendipitously or derived from native proteins and peptide fragments that can self-aggregate *in vivo*, such as EAK 16 from a Z-DNA binding protein and FF-containing fragments from amyloid peptides.[15−19] It is still a formidable challenge to rationally design peptides that can self-assemble to targeted structures and even functions.

We recently demonstrated the crucial role of β-sheet hydrogen bonding in the one-dimensional growth of peptide assembly and its interplay with hydrophobic interactions.[20] We also designed and synthesized several short self-assembling peptides. Given that short peptides are favorable for practical applications because of the relative ease of their large-scale production and purification, they have been exploited as antibacterial and anticancer agents or as templates for the biomimetic synthesis of silica nanomaterials.[21−26] Other advantages of short-assembling peptides lie in the easy establishment of the relationship between molecular structure and assembly and the rational interpretation of the various noncovalent interactions, in contrast to large and complex peptides and proteins.

Here, we design and synthesize three short peptides, i.e., Ac-IIIIKK-CONH₂ (I_4K_2), Ac-IIKKII-CONH₂ ($I_2K_2I_2$), and Ac-KIIIIK-CONH₂ (KI_4K). These have the same amino acid

composition but different sequences. We demonstrate that the simple variation in sequence leads to drastic changes in their assembly, which are well-correlated with the contributions of the various noncovalent forces and their interplay. Such a study would enhance our mechanistic understanding of the peptide self-assembly, thus favoring the design of self-assembling peptides in a rational way.

2. EXPERIMENTAL SECTION

2.1. Materials. The three peptides were synthesized on a CEM Liberty microwave synthesizer based on the standard Fmoc solid-phase synthesis strategy. The Rink amide resin was used to allow for the C terminus to be amidated, and the N terminus was capped with acetic anhydride prior to cleavage from the resin. Detailed synthesis and purification procedures have been described in our previous work.[20,21] The final products were subjected to matrix-assisted laser desorption/ionization time-of-flight mass spectrometry (MALDI–TOF MS) and reversed-phase high-performance liquid chromatography (RP-HPLC) analyses, indicating high purities (98%, Figure S1 and Figure S2).

2.2. Sample Preparation. The purified peptides were dissolved in Milli-Q water to create solutions at a concentration of 16 mM. After sonication for about 5 min, the peptides were completely dissolved and the pH value of the solutions was carefully adjusted to 3.0 using dilute HCl. The resulting homogeneous solutions were incubated for 12 days at room temperature before further characterization.

2.3. Circular Dichroism (CD). The CD measurements were performed on a MOS-450 spectrometer (Biologic, France) using a 0.1 mm path-length quartz cuvette. The CD spectra were recorded at room temperature with wavelengths ranging from 190 to 250 nm and a scan speed of 50 nm min^{-1}. The bandwidth was set to 0.5 nm, and a Xe lamp was used as the light resource. Using the Biokine software package, the solvent background was subtracted and the spectra could be smoothed. The resultant CD signals were expressed as $[\theta]$ (deg cm^2 dmol^{-1}) versus wavelength.

2.4. Cryogenic Transmission Electron Microscopy (Cryo-TEM). Samples for cryo-TEM characterization were prepared in a controlled environment vitrification system (CEVS). A small volume (~5 μL) of aged peptide solution was dropped onto a TEM copper grid coated with a laced support film and then wicked away with two pieces of filter paper, resulting in a thin film suspended on the mesh holes. After about 3 s, the samples were quickly plunged into a reservoir of liquid ethane (cooled by the nitrogen) at −165 °C. Then, the vitrified samples were stored in the liquid nitrogen before transferring to the cryogenic sample holder (Gatan 626) and examined on a JEOL JEM-1400 transmission electron microscope at about −174 °C with an accelerating voltage of 120 kV.

2.5. Negative-Stain Transmission Electron Microscopy (TEM). TEM micrographs were recorded on a JEOL JEM-2100 UHR electron microscope with an accelerating voltage of 200 kV. For sample preparation, a small volume (~10 μL) of aged peptide solution was dropped on a 300-mesh copper grid and allowed to adsorb for 5 min before excess peptide solution was wicked away with a filter paper. Then, the grid was negatively stained with uranyl acetate (2%, w/v) aqueous solution for about 3 min, and excess solution was removed with a filter paper.

2.6. Atomic Force Microscopy (AFM). AFM measurements were performed with a commercial Nanoscope IVa MultiMode atomic force microscope (Digital Instruments, Santa Barbara, CA) in tapping mode. Samples were prepared by dropping a small volume (~10 μL) of aged peptide solution onto a freshly cleaved mica surface and allowed to adsorb for about 30 s. Then, the mica surface was rinsed with water and dried gently with nitrogen gas. The scan rate was set to 1.50 Hz, and the scan angle was set to 0°. All images were flattened using a first-order line fit (the flatten function in AFM software) to correct for piezo-derived differences between scan lines.

2.7. Small-Angle Neutron Scattering (SANS). SANS experiments were carried out at LOQ, ISIS Neutron Facility, Rutherford Appleton Laboratory (Oxford, U.K.). The samples for this experiment

were dissolved in D$_2$O. The solution pH value was then adjusted to 3.0 using DCl solutions in D$_2$O. The resulting homogeneous solutions were incubated for 12 days and then transferred into 2.0 mm path-length disc-shaped silica cells for characterization. Neutron incident wavelengths were from 2.2 to 10.0 Å at 25 Hz. The 64 cm^2 detector with 5 mm resolution was placed at a distance of 4.05 m from the samples, giving a wave vector (q) range of 0.006−0.24 Å^{-1}. Data were corrected for the wavelength dependence of the incident spectrum, the measured sample transmission, and relative detector efficiencies, prior to subtraction of the solvent background (D$_2$O). Absolute scaling was obtained by comparing to the scattering from a partially deuterated polystyrene standard. The data were fitted using the SansView 2.1.1 program provided by RAL.

In the lamellar model, the scattering intensity $I(q)$ can be approximately expressed as

$$I(q) \approx 2\pi(\Delta\rho)^2\varphi\delta/q^2 \propto q^{-2} \tag{1}$$

where δ is the bilayer thickness, φ is the volume fraction, and $\Delta\rho$ is the difference of scattering length densities of the lamellar layers and the surrounding solvent.[27,28]

In the flexible cylinder ellipsoidal model, $I(q)$ can be defined as

$$I(q, L, b, R_{CS}) = c\Delta\rho^2 MS(q, L, b)P(q, R_{CS}) \tag{2}$$

where L is the contour length, b is the statistical segment length (Kuhn length), R_{CS} is the radius of the cross-section, c is the peptide concentration, and M gives the average molecular weight of the assembly. The structure factor $S(q, L, b)$ and the form factor $P(q, R_{CS})$ are given by eqs 3−5[29,30]

$$P(q, R_{CS}) = \left[\frac{2J_1(qR_{CS})}{qR_{CS}}\right]^2 \tag{3}$$

$$S_{(q,L,b)} = S_{exv}(q, L, b) + C(L/b)\left[\frac{4}{15} + \frac{7}{15u} - \left(\frac{11}{15} + \frac{7}{15u}\right)\right.$$
$$\left.\exp(-u)\right]b/L \tag{4}$$

$$S_{exv(q)} = [1 - w(qR_g)]S_{Debye}(q, L, b) + w(qR_g)$$
$$[C_1(qR_g)^{-1/\nu} + C_2(qR_g)^{-2/\nu} + C_3(qR_g)^{-3/\nu}] \tag{5}$$

where $J_1(x)$ denote the Bessel function of the first kind, S_{exv} means that it is for excluded volume effects, and S_{Debye} means the Debye function.

In the hollow cylinder model, $P(q)$ is given in eq 6, where (scale) is a scale factor and H is half of the length of the cylinder. More information about the model is described in ref 31.

$$P(q) = (\text{scale})V_{shell}(\Delta\rho)^2$$
$$\int_0^1 \psi^2[q, R_{shell}(1 - x^2)^{1/2}, R_{core}(1 - x^2)^{1/2}]$$
$$\left[\frac{\sin(qHx)}{qHx}\right]^2 dx \tag{6}$$

2.8. Fluorescence Measurements. Fluorescence measurements for aged peptide solutions and thioflavin T (ThT, 0.05 mM) mixtures were carried out on a Horiba Jobin Yvon Fluoromax-4 spectrometer at ambient temperature. Emission spectra were collected from 450 to 550 nm with an excitation wavelength of 440 nm. The excitation and emission slits were set to 5 and 2.5 nm, respectively.

2.9. Simulation Details. In this work, we have performed a series of explicit-solvent all-atom molecular dynamics (MD) simulations of I$_4$K$_2$ and KI$_4$K monomers and trimers using the GROMAS software.[32] The peptides were modeled by the all-atom optimized potentials for liquid simulations (OPLS-AA) force field,[33] and the tip4p model[34] was used for water molecules. Because the side chain of lysine has a net charge of +1, chloride ions were added to make the system charge neutral. The simulations of monomers were conducted in a *NPT*

ensemble with a periodic boundary condition. The systems were equilibrated for 0.5 ns before 5 ns equilibrium simulations were conducted and sampled. In each simulation of trimers, the system first underwent an energy minimization process using the steepest descent optimization method and then the solvent was relaxed for 0.5 ns in a *NPT* ensemble with the trimer fixed. Finally, a 5 ns constant *NPT* MD simulation was performed and sampled with the trimer released. In all of the above simulations, the time step was 1 fs and 1000 instantaneous conformations were evenly sampled for equilibrium runs. The electrostatic interactions were calculated using the particle mesh Ewald (PME) method.[35,36] Both the van der Waals (VDW) interaction and the real part of the electrostatic interaction had a cutoff of 1.2 nm. The Nosé–Hoover thermostat[37,38] with a coupling time of 0.1 ps was used to keep the system at a constant temperature of 300 K, and the Parrinello–Rahman barostat with a coupling time of 0.5 ps was used to keep the system at a constant pressure of 1 bar.

3. RESULTS AND DISCUSSION

As shown in Table S1 of the Supporting Information, the designed peptides contain four isoleucine (I) residues and two lysine (K) residues and differ only in sequence; both the C and N termini of the three peptides were capped. The choice of I is for its relatively high hydrophobicity and propensity for forming a β-sheet structure,[39,40] while the choice of K is for its cationic charge and close relationship with biosilicification.[24−26] For all of the experiments, the peptide concentration was fixed at 16 mM and the solution pH value was adjusted to around 3.0 by dilute HCl solution. Under such conditions, the peptides were 100% protonated and each molecule carried two positive charges.

First, CD was used to characterize possible molecular conformations after self-assembly of the three peptides. Both I_4K_2 and KI_4K predominantly adopted a β-sheet secondary structure within their assemblies, as indicated by the negative CD minima at about 217 nm (arising from the $n−\pi^*$ transition) (Figure 1). In contrast, $I_2K_2I_2$ was most likely to take a random-coil conformation. This difference implies that they would have different self-assembling behaviors.
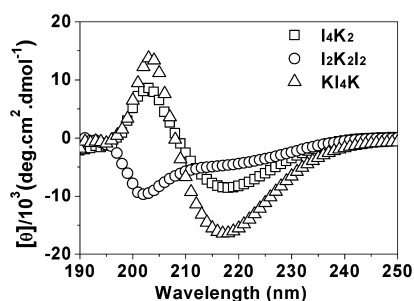
Figure 1. CD spectra of 16 mM I_4K_2, $I_2K_2I_2$, and KI_4K in H_2O at pH 3.0. Prior to CD characterization, the peptide solutions were incubated for 12 days at room temperature. The solvent spectra were subtracted as the background.

Our previous investigation has demonstrated that β-sheet conformations favor the axial growth of peptide assembly because of the alignment of β-strands via hydrogen bonding, leading to the formation of one-dimensional assemblies, such as fibrils and tubes.[20] Consistent with this result, I_4K_2 assembled in aqueous solution into long fibrils with diameters of 10−15 nm and KI_4K formed long nanotubes with diameters in the range of 80−160 nm, as demonstrated by the cryo-TEM (imaged close to the native solvated state[41,42]) and negative-stain TEM characterizations (Figure 2). Note that the tubular
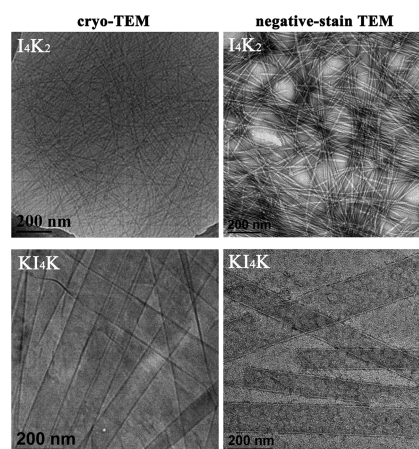

Figure 2. Cryo-TEM and negative-stain TEM micrographs of the assemblies formed by 16 mM I_4K_2 and KI_4K in H_2O at pH 3.0. The peptide solutions were incubated for 12 days at room temperature before characterization. The samples for cryo-TEM characterization were subjected to the vitrification treatment. The samples for negative-stain TEM characterization were negatively stained with an aqueous solution of 2% uranyl acetate.

feature of the observed KI_4K assemblies was verified by their clear dark edge lines in the cryo-TEM image and white edge lines in the negative-stain TEM image.[41,42] In contrast, we were unable to observe well-ordered supramolecular architectures in the $I_2K_2I_2$ aqueous solution using the combination of cryo-TEM and dynamic light scattering techniques. Furthermore, the ThT binding assay indicated that, upon interacting with the I_4K_2 assembles, this dye showed a dramatic increase in fluorescence emission at around 480 nm (Figure 3A). This suggests that I_4K_2 assembles into amyloid-like fibrils, in which the β-strands are aligned perpendicular to both the long axis of the assembly and the lamination of multiple β-sheets.[43−45] Although KI_4K also adopts a β-sheet structure when self-assembling, a relatively weak enhancement in ThT fluorescence emission occurred upon interacting with the peptide assembles (Figure 3A). Such a difference in fluorescence enhancement has been observed by Shao et al. when peptide−dendron hybrids interconvert between fibrillar and nanotube aggregates.[46] These results are indicative of different packing geometries of β-sheets for the I_4K_2 and KI_4K assemblies. For the $I_2K_2I_2$ assemblies, there was no enhanced ThT fluorescence emission at around 480 nm (Figure 3A), because of the absence of a predominant β-sheet structure and/or fibrillar morphology.

Subsequently, we probed the structures of the peptide assemblies at shorter scale lengths using SANS. For I_4K_2 and KI_4K, the SANS intensity (I) versus wave vector (q) followed an approximate −2 dependence, i.e., $I \propto q^{−2}$, which is characteristic of lamellae (Figure 3B).[47−49] This observation indicates that the fundamental unit of the two peptide assemblies is comprised of a lamellar structure. However, the difference between the two plots at q less than 0.1 suggests distinctly higher order assembly and/or nanostructuring of the lamellae. Further data analysis indicated that a flexible cylinderical ellipsoid model plus a lamellar model could provided the best fit to the measured I_4K_2 SANS profile (Figure 3B), giving a fibril diameter of some 12.6 nm and a lamellar thickness of some 1.7 nm. The former is in good agreement with the above value measured from TEM, and the latter is close to the simulated molecular length (around 1.9
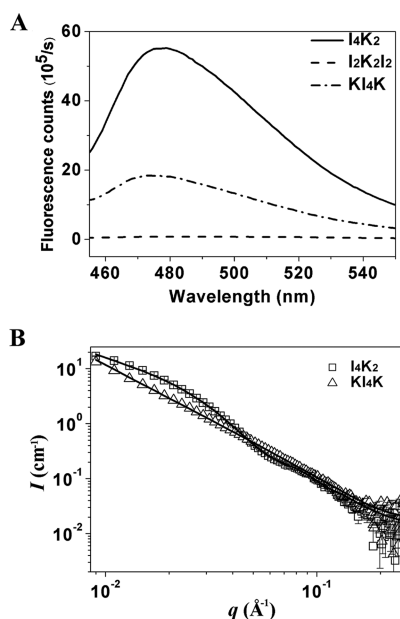
Figure 3. (A) Fluorescence emission spectra (excitation at 440 nm) of 50 μM ThT in the absence and presence of 16 mM peptides: ThT + I$_4$K$_2$ (solid line), ThT + I$_2$K$_2$I$_2$ (dashed line), and ThT + KI$_4$K (dashed-dotted line). Note that there was no fluorescence contribution from ThT alone or the peptide alone in the indicated wavelength range. (B) SANS profiles of 16 mM I$_4$K$_2$ (square) and KI$_4$K (triangle) after 12 days of incubation at pH 3.0. The solid lines are the best fits with the models and parameters given in the text. For clarity, error bars are shown here for the I$_4$K$_2$ data only.

nm, as shown in Figure S3 of the Supporting Information) of I$_4$K$_2$ with a β-strand conformation. In contrast, the combination of a hollow cylinder model and a lamellar model provided the best fit to the measured profile of KI$_4$K well (Figure 3B), producing an outer radius of some 45.0 nm and a wall thickness of some 1.9 nm for the hollow cylinder and a lamellar thickness of some 1.9 nm. The measured nanotube diameter of 90.0 nm in solution from SANS is within the range of 80−160 nm measured in the above TEM characterization. Importantly, the nanotube wall thickness is identical to the lamellar thickness, and both are close to the simulated molecular length (around 2.1 nm, as shown in Figure S3 of the Supporting Information) of KI$_4$K with a β-strand conformation, clearly suggesting that lamellar fragments act as the precursor of the nanotubes and that the wall is comprised of a single lamellar layer. Furthermore, the calculated scattering length densities (SLDs) of I$_4$K$_2$ lamellae, I$_4$K$_2$ nanofibrils, KI$_4$K lamellae, and KI$_4$K nanotubes are all about 3.75×10^{-6} Å^{-2}, consistent with the notion that the higher order assemblies (fibrils and tubes) are composed of lamellae. In addition, on the basis of the calculated SLDs, we can further estimate the peptide volume fraction within these assemblies to be around 56% by taking the SLD of the peptide in D$_2$O to be 1.72×10^{-6} Å^{-2}, with the remaining 44% being occupied by the solvent (water). All of the parameters for the above fitting are given in Table S2 of the Supporting Information. In contrast, no aggregation could be detected from the SANS data of I$_2$K$_2$I$_2$.

On the basis of the above experimental observations, we can reasonably hypothesize the lamellar fragments resulted from the stacking of β-sheets with no or limited residue shifting between neighboring strands, with their thickness close to the molecular length. Therefore, we carried out preliminary MD simulations

to assess the possible molecular arrangements within antiparallel and parallel β-sheets during the early stage of self-assembly. Considering current computer capability and the fact that a strand forms different hydrogen bonds with its two adjacent strands in a β-sheet conformation, all-atom simulations were performed on trimers with different β-sheet conformations (see Figures S4 and S5 of the Supporting Information). The simulation of I$_4$K$_2$ or KI$_4$K monomer in a random conformation served as a reference to understand conformational changes during trimerization. As shown in Table 1

Table 1. Structural Arrangements and Nonbonded Potential Energies of Peptide Trimers with Antiparallel Conformations and Monomers[a]

| molecular arrangement	nonbonded energies (kJ/mol)		number of hydrogen bonds	
	average	standard deviation	average	standard deviation
KI$_4$K trimer antiP_sh0	1452.84	37.15	10.61	1.09
antiP_sh1_sam	1455.16	29.93	10.67	0.98
antiP_sh1_sym_N	1494.95	36.22	9.13	0.96
antiP_sh1_sym_C	1427.14	31.19	10.93	0.91
antiP_sh2_sam	1557.32	39.71	7.44	1.22
antiP_sh2_sym_N	1601.48	37.57	6.29	0.9
antiP_sh2_sym_C	1491.08	40.71	9.26	0.82
KI$_4$K monomer	604.98	18.10	0	0
I$_4$K$_2$ trimer antiP_sh0	1448.92	36.21	10.61	1.09
antiP_sh1_sam	1473.85	39.71	10.67	0.98
antiP_sh1_sym_N	1505.65	33.96	9.13	0.96
antiP_sh1_sym_C	1461.77	37.1	10.93	0.91
antiP_sh2_sam	1561.43	39.75	7.44	1.22
antiP_sh2_sym_N	1591.55	31.05	6.29	0.9
antiP_sh2_sym_C	1562.58	45.99	9.26	0.82
I$_4$K$_2$ monomer	651.65	17.22	0	0

[a]"antiP" means antiparallel; "sh$n$" means shifted alignment of two neighboring monomers with n residues; "sam" means the two neighboring monomers shift in the same direction; "sym" means the top and bottom monomers are symmetric with respect to the middle monomer; and "N" ("C") means the N-terminal (C-terminal) of the monomer in the middle is exposed (see Figure S4 of the Support Information for detailed conformations).

(antiparallel) and Table S3 of the Supporting Information (parallel), the nonbonded potential energies of trimers are always significantly lower than 3 times those of monomers, suggesting that there is a strong driving force for the two peptides to assemble into β-sheet structures. Because hydrogen bonding is responsible for β-sheet formation and stabilization, we also present the number of hydrogen bonds in Table 1 and Table S3 of the Supporting Information. On the basis of the nonbonded energies and the number of hydrogen bonds, the one-residue-shift arrangement (antiP_sh1_sym_C) of KI$_4$K and the zero-residue-shift arrangement (antiP_sh0) of I$_4$K$_2$ are most likely to appear in their β-sheet structures.

Upon forming β-sheets, the amino acid side chains are distributed on either side. The resulting side chain attractions (mainly the hydrophobic interaction) cause the β-sheets to stack laterally and form lamellae. Thus, their thicknesses must be equal to those of their constituted β-sheets and close to the molecular length of peptides constrained in a β-sheet conformation, and the KI$_4$K β-sheet should have a slightly larger thickness than the I$_4$K$_2$ β-sheet because of one residue shift. These are well-consistent with the above experimental
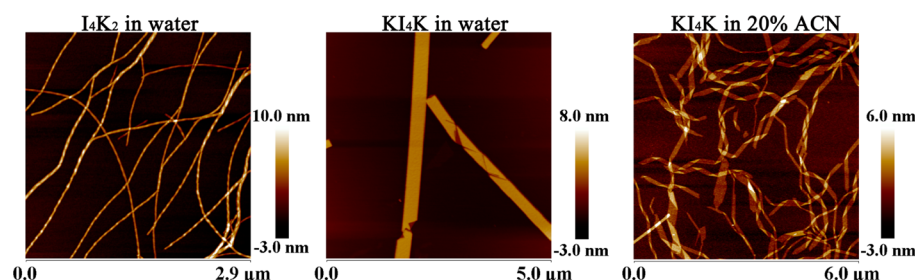
Figure 4. Tapping-mode AFM height images of the assemblies formed by 16 mM I_4K_2 in water and 16 mM KI_4K in water and the mixture of acetonitrile (ACN) and water (1:4, v/v). All samples were prepared by directly dissolving the peptide in the solvents, and then the solution pH was slightly adjusted to 3.0. The peptide solutions were incubated for about 12 days at room temperature before AFM characterization.
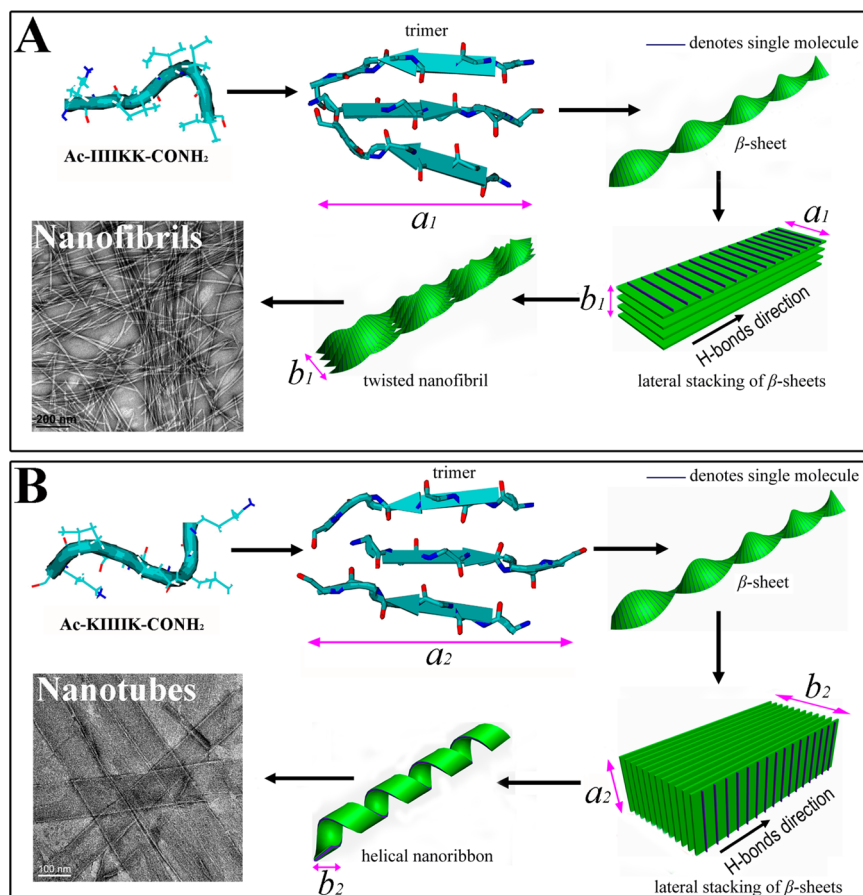
Figure 5. Schematic representation of the hierarchical self-assembly processes of (A) I_4K_2 and (B) KI_4K, consisting of three main steps, i.e., the formation of β-sheets, the lateral stacking of β-sheets, and the evolution of stacked β-sheets into nanofibrils or nanotubes because of inherently twisting of β-sheets. a_1 and a_2, thicknesses of β-sheets, which are equal to those of the lamellae arising from their stacking; b_1 and b_2, lamination of β-sheets.

observations. However, because of the inherent chirality of peptides, the equilibrium structure of the β-sheets is naturally twisted, and when stacking laterally, the primary β-sheets have to reduce their twisting in response to the packing constraints imposed by their twisted neighbors, as suggested by Nyrkova and co-workers.[50−52] Accordingly, these workers have proposed a hierarchical model to describe the formation of self-assembling peptide (DN1: Ac-QQRFQWQFEQQ-CONH$_2$) fibrils, in which peptide monomers undergo a series of consecutive events, including their conformational evolution into rod-like β-strands, the formation of intermolecular β-sheets, and the lateral stacking of twisted β-sheets into cylindrical fibrils. Stupp et al. also suggested that the natural

twisting of β-sheets can be readily accommodated within a cylindrical aggregate.[48,53] The fibril diameter is determined by a balance between the gain in attraction energy associated with stacking and the elastic energy cost for untwisting β-sheets from their natural state.[50−52]

In the case of I_4K_2, the two protonated lysine residues are at the C terminus and, thus, asymmetric along a β-strand. For such a primary structure, the intermolecular electrostatic repulsion of charged lysine side chains must comprise the attraction energy both between β-strands and β-sheets. Note that the hydrophobic interaction, arising from the close contact of isoleucine side chains, is the main contribution to the attraction energy for lateral stacking. As a result, the stacking of

β-sheets has rather limited growth in width and is more twisted. After sufficient incubation time, such as 12 days in this case, the long and narrow twisted stacks (lamellae) develop into fibrils without evident twisting markings and with a relatively uniform diameter of 10−15 nm. Furthermore, this primary molecular geometry is similar to that of conventional ionic surfactants, favoring a curved formation, and the fibrillar morphology also reduces the exposure of the hydrophobic moieties to water. Interestingly, when we applied tapping mode AFM to characterize these mature I_4K_2 fibrils on a mica surface, significantly twisted fibrils were widely observed (Figure 4A). This reversible phenomenon is very likely caused partly by substrate interference and partly by a dilution effect from rinsing during the AFM specimen preparation. The whole self-assembly process of I_4K_2 is schematically represented in Figure 5.

For KI_4K, the two protonated lysine residues are at both termini and, thus, symmetric along a β-strand. Despite the existence of the intermolecular electrostatic repulsion, this molecular geometry bearing the repulsive interaction is submissive to the attraction energy between I residues and the overall effect leads to the facilitation of a flat assembled geometry. Because of these favorable interactions among amino acid side chains, the lateral growth of lamellae is significantly increased until equilibrium is reached. The resulting long and wide ribbons tend to curl into helical tubes, as a result of either inherently twisting of β-sheets, shielding of the hydrophobic amino acids from water, or a combination of both. Finally, after fusing of the edges of helical ribbons, nanotubes with a seamless surface and diameters of 80−160 nm are formed (Figure 5). Similar to the case of I_4K_2, when we applied AFM to characterize the KI_4K nanotubes, their helical markings were clearly observed (Figure 4B). Because organic solvents can effectively decrease the hydrophobic attraction, narrow and helical KI_4K ribbons were widely observed in a 1:4 (v/v) mixture of acetonitrile and water (Figure 4C). The section analysis of these helical ribbons revealed a thickness of around 2.1 nm (see Figure S6 of the Supporting Information), consistent with the wall thickness measured from SANS, further confirming the above notion that the helical ribbons act as the precursor of the nanotubes. Because the two values are close to the simulated molecular length (see Figure S3 of the Supporting Information), we reason that the wall of the nanotubes is comprised of a single lamellar layer, which corresponds to the lateral stacking of the antiparallel β-sheets.

4. CONCLUSION

We have demonstrated that simple sequence variations of amphiphilic hexapeptides ($I_2K_2I_2$, I_4K_2, and KI_4K) with the same amino acid composition can produce different higher order self-assembled architectures. These structural changes have been well-correlated with the interplay of the noncovalent forces (hydrogen bonding, hydrophobic interaction, and electrostatic repulsion) coupled with different molecular geometries. Intermolecular β-sheet hydrogen bonding drives the one-dimensional growth of the assembly, and amino acid side chain interactions (the hydrophobic and electrostatic interactions) are mainly responsible for the lateral growth. Their collective action determines the final assembled nanostructures. In the case of I_4K_2, the electrostatic repulsion acted on the asymmetric molecular geometry served to weaken the hydrophobic attraction between β-sheets, thus leading to their limited stacking and significant twisting, eventually giving

rise to the fibrillar morphology. In the symmetric molecular geometry of KI_4K, the hydrophobic attraction was little influenced by the electrostatic repulsion, resulting in the formation of the wide ribbons that slowly developed into the nanotubes. In contrast, because of the lack of the alignment induced by the β-sheet hydrogen bonding, no well-defined self-assembled structure formed from $I_2K_2I_2$.

Such a mechanistic study would favor the future design of self-assembling peptides in a rational way. Furthermore, because of the low manufacturing cost of short peptides, we envisage that their assembled nanostructures could act as versatile platforms for a variety of technological applications, such as scaffolds for cell culture, templates for functional materials, and vectors for controlled delivery, in contrast to synthetic polymers and large proteins, whose assembled architectures are usually difficult to harness.

■ ASSOCIATED CONTENT

⑤ Supporting Information

Key physicochemical parameters of the three peptides, their RP-HPLC profiles and MALDI−TOF mass spectra, end-to-end distance of KI_4K and I_4K_2 molecules, different arrangements of trimers with antiparallel and parallel β-sheet conformations, and also nonbonded potential energies of peptide trimers with parallel conformations and monomers. This material is available free of charge via the Internet at http://pubs.acs.org.

■ AUTHOR INFORMATION

Corresponding Authors

*E-mail: xuh@upc.edu.cn.
*E-mail: j.lu@manchester.ac.uk.

Notes

The authors declare no competing financial interest.

■ REFERENCES

(1) Lehn, J. M. Toward self-organization and complex matter. *Science* **2002**, *295*, 2400−2403.
(2) Whitesides, G. M.; Grzybowski, B. Self-assembly at all scales. *Science* **2002**, *295*, 2418−2421.
(3) Whitesides, G. M.; Boncheva, M. Beyond molecules: Self-assembly of mesoscopic and macroscopic components. *Proc. Natl. Acad. Sci. U. S. A.* **2002**, *99*, 4769−4774.
(4) Zhang, S. Fabrication of novel biomaterials through molecular self-assembly. *Nat. Biotechnol.* **2003**, *21*, 1711−1178.
(5) Gazit, E. Self-assembled peptide nanostructures: The design of molecular building blocks and their technological utilization. *Chem. Soc. Rev.* **2007**, *36*, 1263−1269.
(6) Ulijn, R. V.; Smith, A. M. Designing peptide based nanomaterials. *Chem. Soc. Rev.* **2008**, *37*, 664−675.
(7) Yan, X.; Zhu, P.; Li, J. Self-assembly and application of diphenylalanine-based nanostructures. *Chem. Soc. Rev.* **2010**, *39*, 1877−1890.

(8) Zhao, X.; Pan, F.; Xu, H.; Yaseen, M.; Shan, H.; Hauser, C. A. E.; Zhang, S.; Lu, J. R. Molecular self-assembly and applications of designer peptide amphiphiles. *Chem. Soc. Rev.* **2010**, *39*, 3480−3498.

(9) Cui, H.; Webber, M. J.; Stupp, S. I. Self-assembly of peptide amphiphiles: From molecules to nanostructures to biomaterials. *Biopolymers* **2010**, *94*, 1−18.

(10) Hamley, I. W. Self-assembly of amphiphilic peptides. *Soft Matter* **2011**, *7*, 4122−4138.

(11) Hauser, C. A. E.; Deng, R.; Mishra, A.; Loo, Y.; Khoe, U.; Zhuang, F.; Cheong, D. W.; Accardo, A.; Sullivan, M. B.; Riekel, C.; Ying, J. Y.; Hauser, U. A. Natural tri- to hexapeptides self-assemble in water to amyloid β-type fiber aggregates by unexpected α-helical intermediate structures. *Proc. Natl. Acad. Sci. U. S. A.* **2011**, *108*, 1361−1366.

(12) Mishra, A.; Loo, Y.; Deng, R.; Chuah, Y. J.; Hee, H. T.; Ying, J. Y.; Hauser, C. A. E. Ultrasmall natural peptides self-assemble to strong temperature-resistant helical fibers in scaffolds suitable for tissue engineering. *Nano Today* **2011**, *6*, 232−239.

(13) Zhuang, F.; Oglęcka, K.; Hauser, C. A. E. Self-assembling peptide surfactants A_6K and A_6D adopt α-helical structures useful for membrane protein stabilization. *Membranes* **2011**, *1*, 314−326.

(14) Lakshmanana, A.; Cheong, D. W.; Accardo, A.; Di Fabrizio, E.; Riekel, C.; Hauser, C. A. E. Aliphatic peptides show similar self-assembly to amyloid core sequences, challenging the importance of aromatic interactions in amyloidosis. *Proc. Natl. Acad. Sci. U. S. A.* **2013**, *110*, 519−524.

(15) Zhang, S.; Holmes, T.; Lockshin, C.; Rich, A. Spontaneous assembly of a self-complementary oligopeptide to form a stable macroscopic membrane. *Proc. Natl. Acad. Sci. U. S. A.* **1993**, *90*, 3334−3338.

(16) Reches, M.; Gazit, E. Casting metal nanowires within discrete self-assembled peptide nanotubes. *Science* **2003**, *300*, 625−627.

(17) Lu, K.; Jacob, J.; Thiyagarajan, P.; Conticello, V. P.; Lynn, D. G. Exploiting amyloid fibril lamination for nanotube self-assembly. *J. Am. Chem. Soc.* **2003**, *125*, 6391−6393.

(18) Yan, X.; He, Q.; Wang, K.; Duan, L.; Cui, Y.; Li, J. Transition of cationic dipeptide nanotubes into vesicles and oligonucleotide delivery. *Angew. Chem., Int. Ed.* **2007**, *46*, 2431−2434.

(19) Krysmann, M. J.; Castelletto, V.; Kelarakis, A.; Hamley, I. W.; Hule, R. A.; Pochan, D. J. Self-assembly and hydrogelation of an amyloid peptide fragment. *Biochemistry* **2008**, *47*, 4597−4605.

(20) Han, S.; Cao, S.; Wang, Y.; Wang, J.; Xia, D.; Xu, H.; Zhao, X.; Lu, J. R. Self-assembly of short peptide amphiphiles: The cooperative effect of hydrophobic interaction and hydrogen bonding. *Chem.—Eur. J.* **2011**, *17*, 13095−13102.

(21) Chen, C.; Pan, F.; Zhang, S.; Hu, J.; Cao, M.; Wang, J.; Xu, H.; Zhao, X.; Lu, J. R. Antibacterial activities of short designer peptides: A link between propensity for nanostructuring and capacity for membrane destabilization. *Biomacromolecules* **2010**, *11*, 402−411.

(22) Chen, C.; Hu, J.; Zhang, S.; Zhou, P.; Zhao, X.; Xu, H.; Zhao, X.; Yaseen, M.; Lu, J. R. Molecular mechanisms of antibacterial and antitumor actions of designed surfactant-like peptides. *Biomaterials* **2012**, *33*, 592−603.

(23) Xu, H.; Chen, C.; Hu, J.; Zhou, P.; Zeng, P.; Cao, C.; Lu, J. R. Dual modes of antitumor action of an amphiphilic peptide A_9K. *Biomaterials* **2013**, *34*, 2731−2737.

(24) Xu, H.; Wang, Y.; Ge, X.; Han, S.; Wang, S.; Zhou, P.; Shan, H.; Zhao, X.; Lu, J. R. Twisted nanotubes formed from ultrashort amphiphilic peptide I_3K and their templating for the fabrication of silica nanotubes. *Chem. Mater.* **2010**, *22*, 5165−5173.

(25) Wang, S.; Ge, X.; Xue, J.; Fan, H.; Mu, L.; Li, Y.; Xu, H.; Lu, J. R. Mechanistic processes underlying biomimetic synthesis of silica nanotubes from self-assembled ultrashort peptide templates. *Chem. Mater.* **2011**, *23*, 2466−2474.

(26) Wang, S.; Xue, J.; Ge, X.; Fan, H.; Xu, H.; Lu, J. R. Biomimetic synthesis of silica nanostructures with controllable morphologies and sizes through tuning interfacial interactions. *Chem. Commun.* **2012**, *48*, 9415−9417.

(27) Porte, G. In *Neutrons, X-rays and Light: Scattering Methods Applied to Soft Condensed Matter*; Lindner, P., Zemb, T., Eds.; Elsevier: Amsterdam, Netherlands, 2002; North-Holland Delta Series.

(28) Glatter, O.; Kratky, O. *Small Angle X-rays Scattering*; Academic Press: New York, 1982.

(29) Pedersen, J. S.; Schurtenberger, P. Scattering functions of semiflexible polymers with and without excluded volume effects. *Macromolecules* **1996**, *29*, 7602−7612.

(30) Chen, W.-R.; Butler, P. D.; Magid, L. J. Incorporating intermicellar interactions in the fitting of SANS data form cationic wormlike micelles. *Langmuir* **2006**, *22*, 6539−6548.

(31) Feigin, L. A.; Svergun, D. I. *Structure Analysis by Small-Angle X-Ray and Neutron Scattering*; Plenum Press: New York, 1987.

(32) Van Der Spoel, D.; Lindahl, E.; Hess, B.; Groenhof, G.; Mark, A. E.; Berendsen, H. J. C. GROMACS: Fast, flexible, and free. *J. Comput. Chem.* **2005**, *26*, 1701−1718.

(33) Jorgensen, W. L.; Tirado-Rives, J. The OPLS potential functions for proteins. Energy minimizations for crystals of cyclic peptides and crambin. *J. Am. Chem. Soc.* **1988**, *110*, 1657−1666.

(34) Jorgensen, W. L.; Chandrasekhar, J.; Madura, J. D.; Impey, R. W.; Klein, M. L. Comparison of simple potential functions for simulating liquid water. *J. Chem. Phys.* **1983**, *79*, 926−935.

(35) Darden, T.; York, D.; Pedersen, L. Particle mesh Ewald: An N·log(N) method for Ewald sums in large systems. *J. Chem. Phys.* **1993**, *98*, 10089−10092.

(36) Essmann, U.; Perera, L.; Berkowitz, M. L.; Darden, T.; Lee, H.; Pedersen, L. G. A smooth particle mesh Ewald method. *J. Chem. Phys.* **1995**, *103*, 8577−8593.

(37) Nose, S. A molecular dynamics method for simulations in the canonical ensemble. *Mol. Phys.* **1984**, *52*, 255−268.

(38) Hoover, W. G. Canonical dynamics: Equilibrium phase-space distributions. *Phys. Rev. A: At., Mol., Opt. Phys.* **1985**, *31*, 1695−1697.

(39) Minor, L. J. D.; Kim, S. P. Measurement of the β-sheet-forming propensities of amino acids. *Nature* **1994**, *367*, 660−663.

(40) Xiong, H.; Buckwalter, B. L.; Shieh, H. M.; Hecht, M. H. Periodicity of polar and nonpolar amino acids is the major determinant of secondary structure in self-assembling oligomeric peptides. *Proc. Natl. Acad. Sci. U. S. A.* **1995**, *92*, 6349−6353.

(41) Friedrich, H.; Frederik, P. M.; de With, G.; Sommerdijk, N. A. J. M. Imaging of self-assembled structures: Interpretation of TEM and cryo-TEM images. *Angew. Chem., Int. Ed.* **2010**, *49*, 7850−7858.

(42) Cenker, Ç. Ç.; Bomans, P. H. H.; Friedrich, H.; Dedeoğlu, B.; Aviyente, V.; Olsson, U.; Sommerdijk, N. A. J. M.; Bucak, S. Peptide nanotube formation: A crystal growth process. *Soft Matter* **2012**, *8*, 7463−7470.

(43) Levine, H. Thioflavine T interaction with synthetic Alzheimer's disease β-amyloid peptides: Detection of amyloid aggregation in solution. *Protein Sci.* **1993**, *2*, 404−410.

(44) Ban, T.; Hamada, D.; Hasegawa, K.; Naiki, H.; Goto, Y. Direct observation of amyloid fibril growth monitored by thioflavin T fluorescence. *J. Biol. Chem.* **2003**, *278*, 16462−16465.

(45) Biancalana, M.; Makabe, K.; Koide, A.; Koide, S. Molecular mechanism of thioflavin-T binding to the surface of β-rich peptide self-assemblies. *J. Mol. Biol.* **2009**, *385*, 1052−1063.

(46) Shao, H.; Parquette, J. R. Controllable peptide–dendron self-assembly: Interconversion of nanotubes and fibrillar nanostructures. *Angew. Chem., Int. Ed.* **2009**, *48*, 2525−2528.

(47) Nieh, M. -P.; Kučerka, N.; Katsaras, J. Spontaneously formed unilamellar vesicles. *Methods Enzymol.* **2009**, *465*, 3−20.

(48) Cui, H.; Muraoka, T.; Cheetham, A. G.; Stupp, S. I. Self-assembly of giant peptide nanobelts. *Nano Lett.* **2009**, *9*, 945−951.

(49) Ziserman, L.; Lee, H.-Y.; Raghavan, S. R.; Mor, A.; Danino, D. Unraveling the mechanism of nanotube formation by chiral self-assembly of amphiphiles. *J. Am. Chem. Soc.* **2011**, *133*, 2511−2517.

(50) Nyrkova, I. A.; Semenov, A. N.; Aggeli, A.; Boden, N. Fibril stability in solutions of twisted β-sheet peptides: A new kind of micellization in chiral systems. *Eur. Phys. J. B* **2000**, *17*, 481−497.

(51) Nyrkova, I. A.; Semenov, A. N.; Aggeli, A.; Bell, M.; Boden, N.; McLeish, T. C. B. Self-assembly and structure transformations in living polymers forming brils. *Eur. Phys. J. B* **2000**, *17*, 499−513.

(52) Aggeli, A.; Nyrkova, I. A.; Bell, M.; Harding, R.; Carrick, L.; McLeish, T. C. B.; Semenov, A. N.; Boden, N. Hierarchical self-assembly of chiral rod-like molecules as a model for peptide β-sheet tapes, ribbons, fibrils, and fibers. *Proc. Natl. Acad. Sci. U. S. A.* **2001**, *98*, 11857−11862.

(53) Jiang, H. Z.; Guler, M. O.; Stupp, S. I. The internal structure of self-assembled peptide amphiphiles nanofibers. *Soft Matter* **2007**, *3*, 454−462.